JCI The Journal of Clinical Investigation

Mapping immune processes in intact tissues at cellular resolution

Christian Brede, … , Gregory S. Harms, Andreas Beilhack

J Clin Invest. 2012;122(12):4439-4446. https://doi.org/10.1172/JCI65100.

Technical Advance **Immunology**

Understanding the spatiotemporal changes of cellular and molecular events within an organism is crucial to elucidate the complex immune processes involved in infections, autoimmune disorders, transplantation, and neoplastic transformation and metastasis. Here we introduce a novel multicolor light sheet fluorescence microscopy (LSFM) approach for deciphering immune processes in large tissue specimens on a single-cell level in 3 dimensions. We combined and optimized antibody penetration, tissue clearing, and triple-color illumination to create a method for analyzing intact mouse and human tissues. This approach allowed us to successfully quantify changes in expression patterns of mucosal vascular addressin cell adhesion molecule–1 (MAdCAM-1) and T cell responses in Peyer's patches following stimulation of the immune system. In addition, we employed LSFM to map individual T cell subsets after hematopoietic cell transplantation and detected rare cellular events. Thus, we present a versatile imaging technology that should be highly beneficial in biomedical research.

Mapping immune processes in intact tissues at cellular resolution

Christian Brede,[1,2,3] Mike Friedrich,[4] Ana-Laura Jordán-Garrote,[1,2,3] Simone S. Riedel,[1,2,3] Carina A. Bäuerlein,[1,2,3] Katrin G. Heinze,[4] Tobias Bopp,[5] Stephan Schulz,[6] Anja Mottok,[7] Carolin Kiesel,[1,3] Katharina Mattenheimer,[1,3] Miriam Ritz,[1,3] Viktoria von Krosigk,[1] Andreas Rosenwald,[7] Hermann Einsele,[1] Robert S. Negrin,[8] Gregory S. Harms,[4] and Andreas Beilhack[1,2,3]

[1]Department of Medicine II, Würzburg University Hospital, Würzburg, Germany. [2]Graduate School of Life Sciences Würzburg, Würzburg, Germany. [3]Interdisciplinary Centre for Clinical Research (IZKF), Würzburg University, Würzburg, Germany. [4]Rudolf Virchow Center, Deutsche Forschungsgemeinschaft (DFG) Research Center for Experimental Biomedicine, Würzburg, Germany. [5]Institute for Immunology, University Medical Center, Johannes Gutenberg-University Mainz, Mainz, Germany. [6]Institute of Pathology, Charité Berlin, Berlin, Germany. [7]Institute of Pathology, Würzburg University, Würzburg, Germany. [8]Department of Medicine, Division of Blood and Marrow Transplantation, Stanford University, Stanford, California, USA.

Understanding the spatiotemporal changes of cellular and molecular events within an organism is crucial to elucidate the complex immune processes involved in infections, autoimmune disorders, transplantation, and neoplastic transformation and metastasis. Here we introduce a novel multicolor light sheet fluorescence microscopy (LSFM) approach for deciphering immune processes in large tissue specimens on a single-cell level in 3 dimensions. We combined and optimized antibody penetration, tissue clearing, and triple-color illumination to create a method for analyzing intact mouse and human tissues. This approach allowed us to successfully quantify changes in expression patterns of mucosal vascular addressin cell adhesion molecule–1 (MAdCAM-1) and T cell responses in Peyer's patches following stimulation of the immune system. In addition, we employed LSFM to map individual T cell subsets after hematopoietic cell transplantation and detected rare cellular events. Thus, we present a versatile imaging technology that should be highly beneficial in biomedical research.

Introduction

A variety of different imaging strategies have been utilized to study immune cell activity and migration in animal models of human disease. Imaging techniques such as MRI, PET, and single-photon emission tomography (SPECT) are particularly attractive, since they can be readily translated from preclinical animal models to clinical application in humans (1). However, these techniques generally do not provide sufficient resolution to visualize individual cells and in many cases lack sensitivity to detect rare biological events in different areas throughout the body. In contrast, high-resolution imaging techniques such as confocal microscopy and multiphoton laser scanning microscopy (MPM) have limited penetration depth due to specimen-induced aberrations and, therefore, do not allow study of the area of interest within a large tissue volume.

So far, enormous efforts have been undertaken to visualize single immune cells throughout the body in murine models of human disease, particularly by high-precision cryosectioning of entire organs, and subsequent compilation of consecutive images (2, 3). This laborious approach provided valuable insights; however, it was prone to tissue distortions and artifacts. Recently, several techniques for morphological and functional imaging have been developed to visualize mesoscopic specimens employing 3D microscopy strategies including optical projection tomography (OPT) (4) and optical coherence tomography (OCT) (5), as well as light sheet–based techniques such as selective plane illumination microscopy (SPIM) (6) and ultramicroscopy (7). So far, light sheet fluorescence microscopy (LSFM) has been employed only in a very few intact adult mouse organs such as the brain (8), spinal cord (9), and the middle ear (10), using single-color illumination. Other microscopy techniques such as OPT and OCT do not achieve cellular resolution (11) or do not allow a multicolor application (12).

In light-sheet microscopy, a tissue-clearing procedure (replacement of water by a more highly refractive index substance) is typically used to make the specimen transparent. Here, we combined deep tissue staining protocols with optimized clearing procedures and advanced LSFM for the first time to be used as a quantitative triple-color technique investigating intact murine and human samples. Complex immune processes, as for instance in hematopoietic cell transplantation or in antitumor responses, can now be analyzed on a single-cell level in large tissue specimens or even entire organs.

Results

A virtual journey through intact tissues by multicolor LSFM. Using LSFM, we imaged Peyer's patches (PPs), which are initiation sites for adaptive immune responses as they occur in infections and autoimmune diseases. We visualized intact PPs of adult mice after specific deep tissue antibody staining and clearing of the tissue specimens (Figure 1, A and B).

Three spectrally distinct light sheets were created for a one-sided illumination, and images were detected sequentially (Figure 1C). Intrinsic autofluorescence in the green color channel provided microanatomical details of the intestinal mucosa and submucosa. Even subepithelial dome regions and B cell follicles of PPs could be visualized and clearly differentiated from adjacent crypts and villi. To highlight T lymphocytes, we stained with red-labeled anti-CD4–Alexa Fluor 647. High endothelial venules (HEVs), which play an important role in lymphocyte entry into PPs, were labeled with

Conflict of interest: The authors have declared that no conflict of interest exists.
Citation for this article: *J Clin Invest.* 2012;122(12):4439–4446. doi:10.1172/JCI65100.

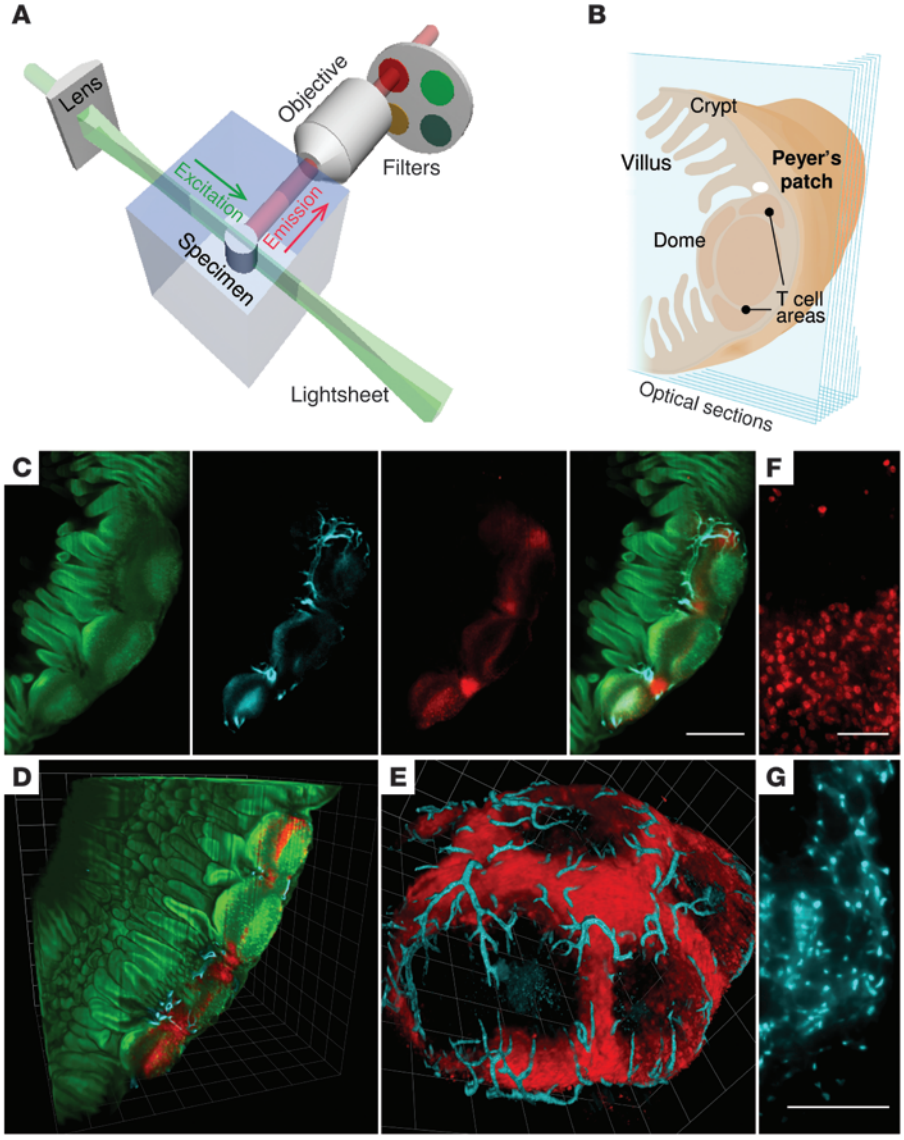

Figure 1
Principle of optical sectioning and computational 3D reconstruction by multicolor LSFM. (**A**) The sample is placed into the chamber with clearing solution and illuminated by laser light sheets of different wavelengths to excite and detect fluorescence (beam path of emission and excitation is indicated by an arrow) in the labeled specimen in 3 detection channels by turning an optical filter wheel. To create optical *z*-stacks, the sample is moved by 1- to 5-μm increments through the light sheet. Assembling *x-y-z* planes allows computational 3D reconstruction. (**B**) Gut-associated PPs are important sites of mucosal immune reactions. (**C**) Imaging of tissue autofluorescence (green) allows for visualization of micro-anatomical features of intact organs such as the small intestinal tract containing a PP with high endothelial venules (MAdCAM-1, cyan) and $CD4^+$ T cells (red) as single and color-merged single optical sections (objective, ×5; scale bar: 100 μm) and (**D**) after computational 3D reconstruction. (**E**) 3D reconstruction of the whole organ reveals co-localization of MAdCAM-1 expression and $CD4^+$ T cells in a PP. Using a ×20 objective allowed a higher magnification of (**F**) single $CD4^+$ T cells (*z*-projection scale bar: 100 μm) and (**G**) subcellular precision imaging single-cell nuclei (stained with DAPI) within lymph nodes (*z*-projection scale bar: 100 μm).

mucosal addressin cell adhesion molecule–1 (MAdCAM-1–Alexa Fluor 546, measured in the yellow color channel). High-precision optical *z*-stacks provided 1,800 optical sections (×5 objective) with an increment of 5 μm and allowed for scanning of whole PPs and lymph nodes (size, >18 mm^3) in 3 color channels within minutes. The resulting *z*-stack required no further image processing and could be directly used for 3D tissue reconstruction (Figure 1, D and E), volume measurements, and quantification of protein expression. This precise 3D tissue reconstruction additionally allowed a virtual journey through the small intestine, which offered unique insights into the whole PP as well as adjacent areas (Supplemental Videos 1 and 2; supplemental material available online with this article; doi:10.1172/JCI65100DS1). Using a ×20 objective enabled us to visualize single $CD4^+$ cells (Figure 1F) and even subcellular components, such as individual nuclei (Figure 1G), deep within the tissue. In our hands, LSFM has proven to have a major acquisition speed advantage over MPM in imaging whole transparent PPs (LSFM <12 minutes, MPM approximately 6 hours; Supplemental Figure 1) and reached a higher penetration depth (LSFM >2 mm).

Application of LSFM in multiple tissues of mice and humans. Labeling of intact tissues with multiple fluorescent antibodies for 3D imaging opens a broad range of biomedical applications, because any molecule of interest can be stained. For optimal analysis of whole organs, a homogeneous and specific antibody staining deep into the tissue is required. To this end, two strategies turned out to be efficient. We injected fluorochrome-labeled antibodies i.v. and shortly thereafter euthanized animals for microscopic analysis. We confirmed the specificity of antibody binding and distribution with immunofluorescence microscopy on frozen sections (Supplemental Figure 2 and Supplemental Figure 3, A and B) and by flow cytometry (Supplemental Figure 3C). Alternatively, we optimized a protocol to stain fixed intact organs that allowed for deep tissue staining. Only the combination of deep tissue antibody staining with sample-clearing procedures allowed visualizing any individual fluorescently labeled cell type within various mouse tissues, such as the heart, testicle, skin, and lymph nodes (Figure 2, A–C, and Supplemental Video 3). The successful imaging of hemoglobin-rich heart and optical dense liver required extra tissue

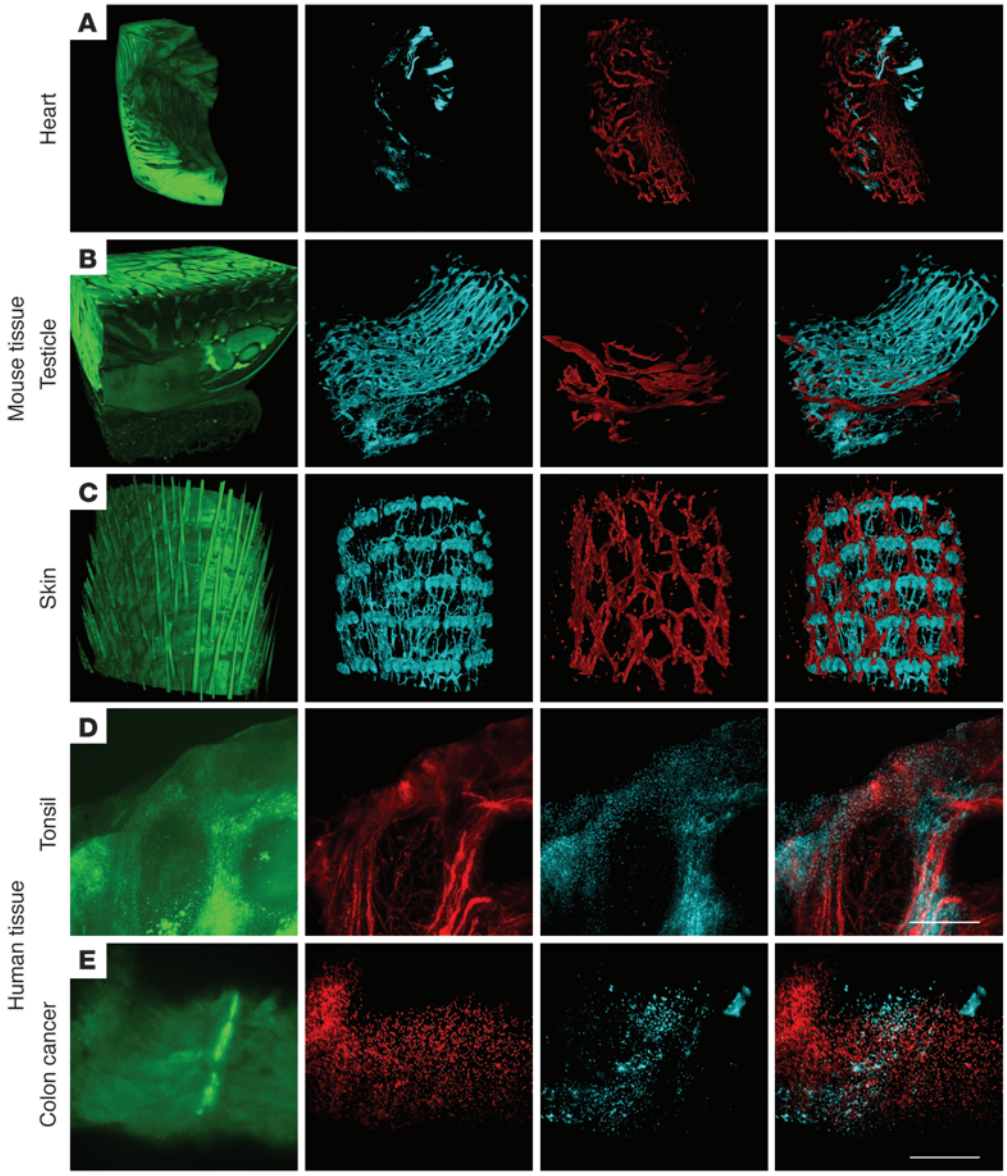

Figure 2
Multicolor LSFM of diverse murine and human tissues. (**A**–**C**) A C57BL/6 mouse was injected i.v. with fluorescently labeled antibodies CD31 (cyan) and LYVE-1 (red). Organs such as (**A**) heart, (**B**) testicle, and (**C**) skin were removed 1 hour after injection and prepared for LSFM. Shown are 3D reconstructions from optical sections imaged with a ×5 objective. (**D** and **E**) LSFM allowed imaging of whole human tissue biopsy samples after modification of the processing procedures. (**D**) *z*-Projection of a human tonsil biopsy (autofluorescence, green) shows the colocalization of CD31 (red) and CD8 (cyan) (scale bar: 500 μm). (**E**) A moderately differentiated human colon adenocarcinoma specimen with tumor-infiltrating $CD8^+$ T cells (red) and $CD4^+$ T cells (cyan) (scale bar: 500 μm).

brightening by peroxidase treatment before sample clearing. In addition to performing studies in the mouse, we applied LSFM to analyze human specimens such as tonsils and colon cancer biopsy samples. Here, we successfully stained and displayed $CD8^+$ T cells in relation to $CD31^+$ endothelial cells in tonsils (Figure 2D) and tumor-infiltrating $CD4^+$ and $CD8^+$ T cells in colon cancer (Figure 2E and Supplemental Figure 4). Of note, the desmoplastic stroma reaction that is often present in cancer samples required modification of the processing procedure to allow antibody access into these very dense tissues.

Quantification of immune processes in entire organs. As LSFM proved valuable for mapping individual immune cells in murine and human tissues, we applied this technique to investigate evolving immune processes by repeated sampling. We used a model of acute GVHD to study T cell interactions with HEVs in whole PPs after allogeneic hematopoietic cell transplantation (allo-HCT) (13). We induced acute GVHD in myeloablatively conditioned BALB/c mice by transplanting bone marrow cells from C57BL/6 ($CD90.2^+$, $CD45.2^+$) donors and luciferase transgenic C57BL/6 $CD45.1^+$ or $CD90.1^+$ T cells. We followed the in vivo progression of GVHD on a macroscopic level by non-invasive bioluminescence imaging (BLI), which pinpointed organs of donor T cell infiltration (Figure 3). At the transition from GVHD initiation to effector phase (day +3 to day +4) (14) and at the first peak of the effector phase (day +6), we prepared PPs (Figure 4) and other tissues (Supplemental Figure 5) of recipients for subsequent whole-organ microscopy. To identify donor T cells, we injected anti-CD45.1– or anti-CD90.1–specific monoclonal antibodies i.v. and stained for the adhesion molecule MAdCAM-1 ex vivo on the fixed tissue. Subsequently, we mapped and quantified the expression of MAdCAM-1 in relation to T cell numbers within PPs in the course of GVHD. Whereas LSFM allows clear identification of single cells from different T cell subsets, automated cell counting was impeded by dense lymphocyte clustering (Supplemental Figure 6A). As a solution, we measured the entire T cell volume in whole PPs and calculated absolute T cell numbers by

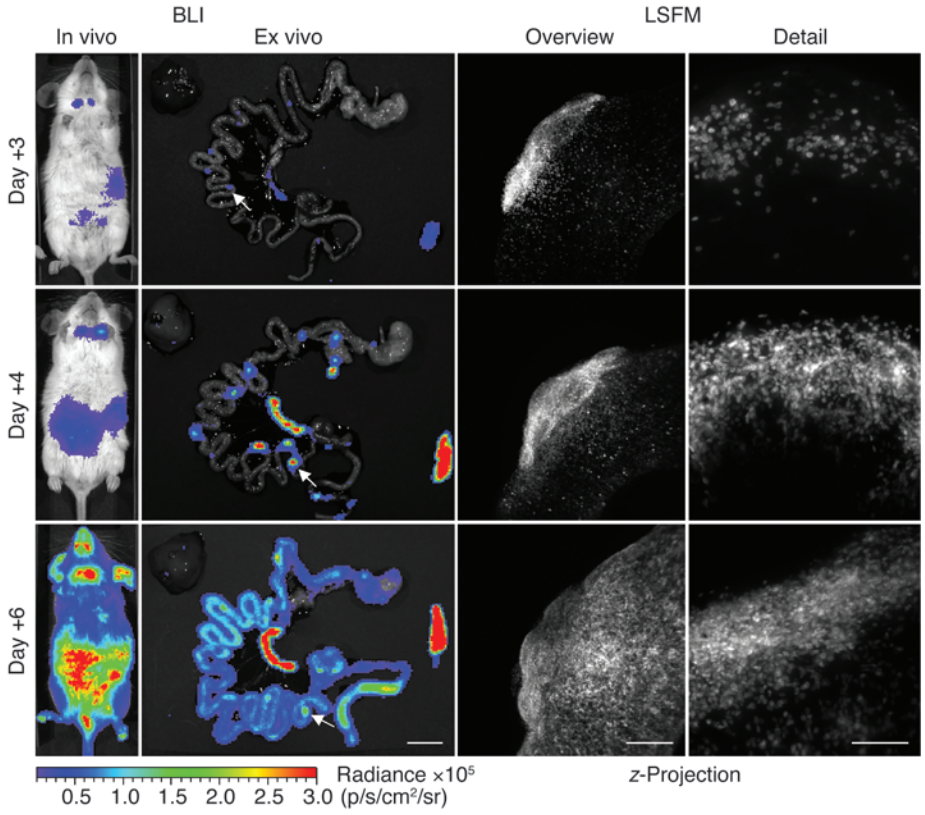

Figure 3
From whole-body bioluminescence to single-cell LSFM imaging. Bone marrow together with luc+CD45.1+ transgenic T cells were transplanted into irradiated allogeneic recipients to induce acute GVHD. Organs (indicated by arrows) were removed at the transition from GVHD initiation phase to effector phase (day +3 and day +4 after allo-HCT) and at the effector phase (day +6) and stained ex situ for donor T cells. Until day +3, the transplanted T cells proliferate within secondary lymphoid organs and start to egress by day +4. Scale bar: BLI 1 cm, LSFM overview 500 μm, and detail LSFM 100 μm. sr, steradian.

using the mean value of the measured cell volume (Supplemental Figure 6, B–F). To avoid inexact enumeration caused by the changing volume of donor T cells due to cell activation, we calculated mean values for day +3, day +4, and day +6 after allo-HCT (Supplemental Figure 6, G–J). The 3D reconstruction of small intestines in healthy mice revealed that the MAdCAM-1 expression averaged approximately 6% of the entire PP and was predominantly restricted to HEVs (Figure 4A). The overall MAdCAM-1 expression in PPs increased by more than 50% during the GVHD initiation phase (days 3–4) and even more during the effector phase on day +6 after allo-HCT. At this point, we found massive MAdCAM-1 upregulation in follicular B cell areas (Figure 4B). Donor T cell numbers in the entire PPs increased between days +3 and +4 (Figure 4C), demonstrating active cell recruitment and proliferation. By day +6 most donor T cells disappeared from the PPs, indicating migration to peripheral GVHD target organs, as confirmed by BLI (Supplemental Figure 7, A and B) and immunofluorescence microscopy of PP cross sections (Supplemental Figure 7, C and D). On days +3 and +4, high numbers of donor T cells also located to MAdCAM-1–positive follicular areas, and they mostly disappeared by day +6.

Visualizing and counting rare events. As we were able to reliably visualize and quantify high numbers of donor T cells in PPs after HCT, we tested whether multicolor LSFM is also capable of detecting rare cellular events. To this end, we adoptively transferred FACS-sorted $CD4^+$ T cell subsets ($CD62L^{hi}CD44^{lo}$ naive T_N cells, $CD62L^{hi}CD44^{hi}$ central memory T_{CM} cells, and $CD62L^{lo}CD44^{hi}$ effector memory T_{EM} cells) (15) from $CD45.1^+$ donors (Figure 5A). Whole PPs and mesenteric lymph nodes (mLNs) of the recipients were analyzed 20 hours after T cell transfer. We established an algorithm that enabled us to automatically identify and count individual cells and found that T_N cells (mean, 726 cells/PP) homed more efficiently than T_{CM} cells (mean, 478 cells/PP) to PPs (Figure 5, B and C) and to mLNs (Supplemental Figure 8). Within the same experiment a comparable homing trend to secondary lymphoid organs (SLOs) was confirmed by FACS analysis of the spleen (data not shown). T_{EM} cells migrate most efficiently to peripheral tissues as opposed to SLOs. In line with this, LSFM revealed low numbers of T_{EM} (mean, 81/PP) homing to PPs (Figure 5, B and C). Most T_{EM} cells located in proximity to MAdCAM-1–expressing HEVs, indicating homing to the T cell zone.

Discussion

Here, we describe a novel multicolor LSFM approach to analyze complex immune processes at the single-cell level in whole organs. Based on optical sectioning, this convenient method required combination of the protocols of optimized antibody penetration, tissue clearing, and multiple color illumination to allow an accurate computational 3D reconstruction of intact tissues. This highly versatile technique allows multicolor imaging of diverse tissue specimens from mice and humans.

LSFM fills the gap between microscopic imaging techniques such as confocal microscopy and macroscopic imaging techniques like MRI or BLI. LSFM thereby circumvents the obstacle of alternative 3D imaging methods such as OPT that are limited by the requirement of time-consuming back-projection (4). A clear advantage of LSFM is that optical sectioning allows rapid screening for rare events in mesoscopic specimens without requiring any image calculation. Therefore, areas of interest can be identified immediately during the acquisition process, which allows for

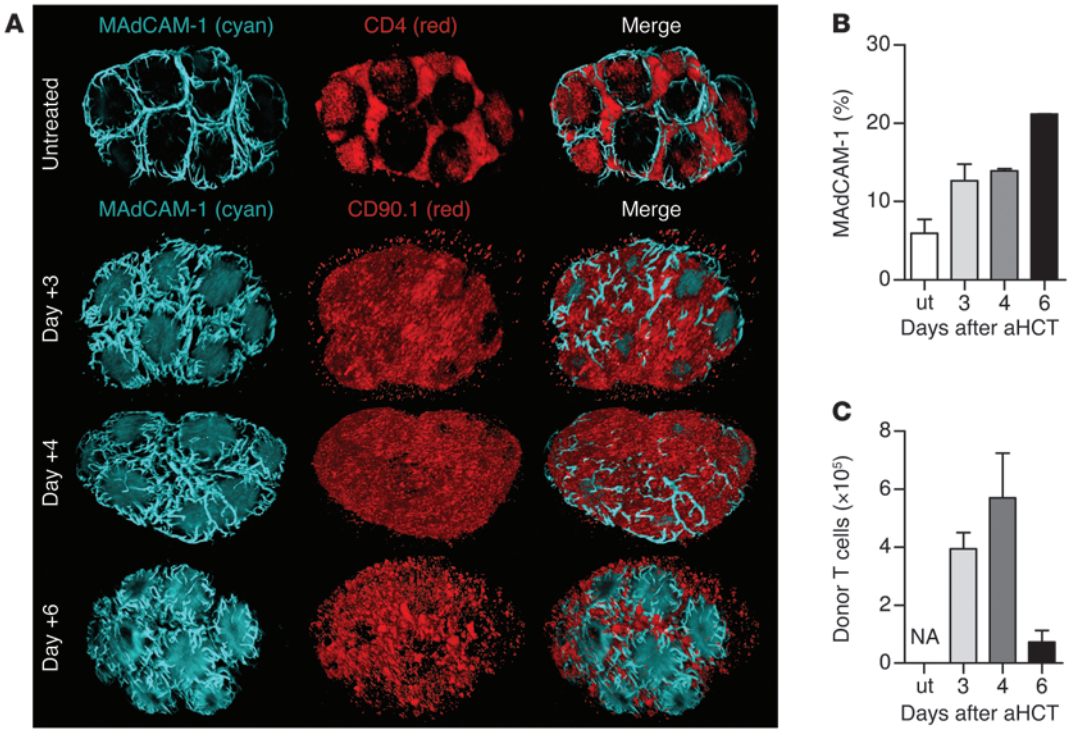

Figure 4

Visualizing and quantifying cellular changes after allo-HCT in 3D. Bone marrow together with CD90.1$^+$ transgenic T cells were transplanted into irradiated allogeneic recipients to induce acute GVHD. CD90.1 or CD4 antibody was injected i.v., and MAdCAM-1 was stained ex situ. (**A**) Representative PPs of untreated and transplant recipient mice highlight differences in MAdCAM-1 expression and numbers of donor T cells. (**B**) After allo-HCT, MAdCAM-1 is highly upregulated in the PPs, particularly in follicular areas. (**C**) Quantification of donor T cells in the entire PP demonstrate proliferation until day 4. By day 6 most donor T cells exit, as confirmed by BLI. Shown is 1 representative experiment of 2 with 2–4 mice per time point.

more focused investigation at higher magnifications. The ability to detect and automatically count rare events in micrometer resolution within large tissue samples, as shown in this study, suggests LSFM as an effective tool to investigate single hematopoietic stem cells (16) or even to identify cancer stem cells (17).

By using a model of acute GVHD, we demonstrated that multicolor LSFM is suitable for visualizing and quantifying cellular changes within whole secondary lymphoid organs (e.g., PPs and mLNs). We found a dramatic upregulation of MAdCAM-1 on HEVs and within follicular areas. It is well established that MAdCAM-1 is an important regulator in lymphocyte homing to PPs via HEVs (18) but is also expressed on MRCs and FDCs (19) and thus is thought to potentially contribute to lymphocyte motility (20). Furthermore, we successfully quantified donor T cell numbers in the entire PPs. With optical sectioning by LSFM alone, these quantifications were not prone to artifacts that occur on cut surfaces. This becomes particularly advantageous when reliable counting of rare cellular events is required and acquiring cryosections may become overly challenging. We investigated the fate of individual CD4$^+$ T cell subsets that either induce (T_N and T_{CM}) or do not induce (T_{EM}) lethal GVHD after allo-HCT (21–23). The mechanisms whereby T_{EM} fail to cause GVHD remain unclear. One controversial hypothesis proposes differences in migration and priming (14, 24), since T_{EM} do not express CD62L and CCR7 and are nearly absent in lymph nodes (25). In line with this, when scanning whole SLOs in high resolution, we quantified low numbers of CD4$^+$ T_{EM} cells homing to T cell areas of PPs and mLNs. Hence, LSFM gave us new insights into migration and dispersal of different T cell subtypes after HCT and should prove useful for optimization of cellular therapies.

Advanced light sheet illumination modes (26, 27) as well as the combination with super-resolution approaches (28) even leave room for future contrast and resolution enhancements. Recent developments to optimize clearing procedures rendering organs transparent, as shown for the central nervous system (9, 29), will further assist in reducing background fluorescence and enhancing fluorescence protein stability. In cleared samples, high tissue autofluorescence, — particularly in the green color channel, caused by formalin fixation (30) — allows the display of detailed microanatomical features. This proved advantageous for locating specific fluorescently labeled cell populations within their anatomical context. However, this strong autofluorescent background noise also poses certain limitations for the utilization of green fluorophores for specific labeling. Therefore, we recommend reliance on fluorophores in the red or near-infrared color spectrum, as demonstrated in this study.

In conclusion, we have shown multicolor LSFM to be a rigorous tool for effectively pinpointing and quantifying rare cellular events and cell-cell interactions within intact organs of mice and humans. Biomedical research that translates scientific progress into clinical approaches should greatly benefit from the application of this high-resolution technology. Therefore, 3D multicolor LSFM holds the promise of complementing classical histopathological diagnosis.

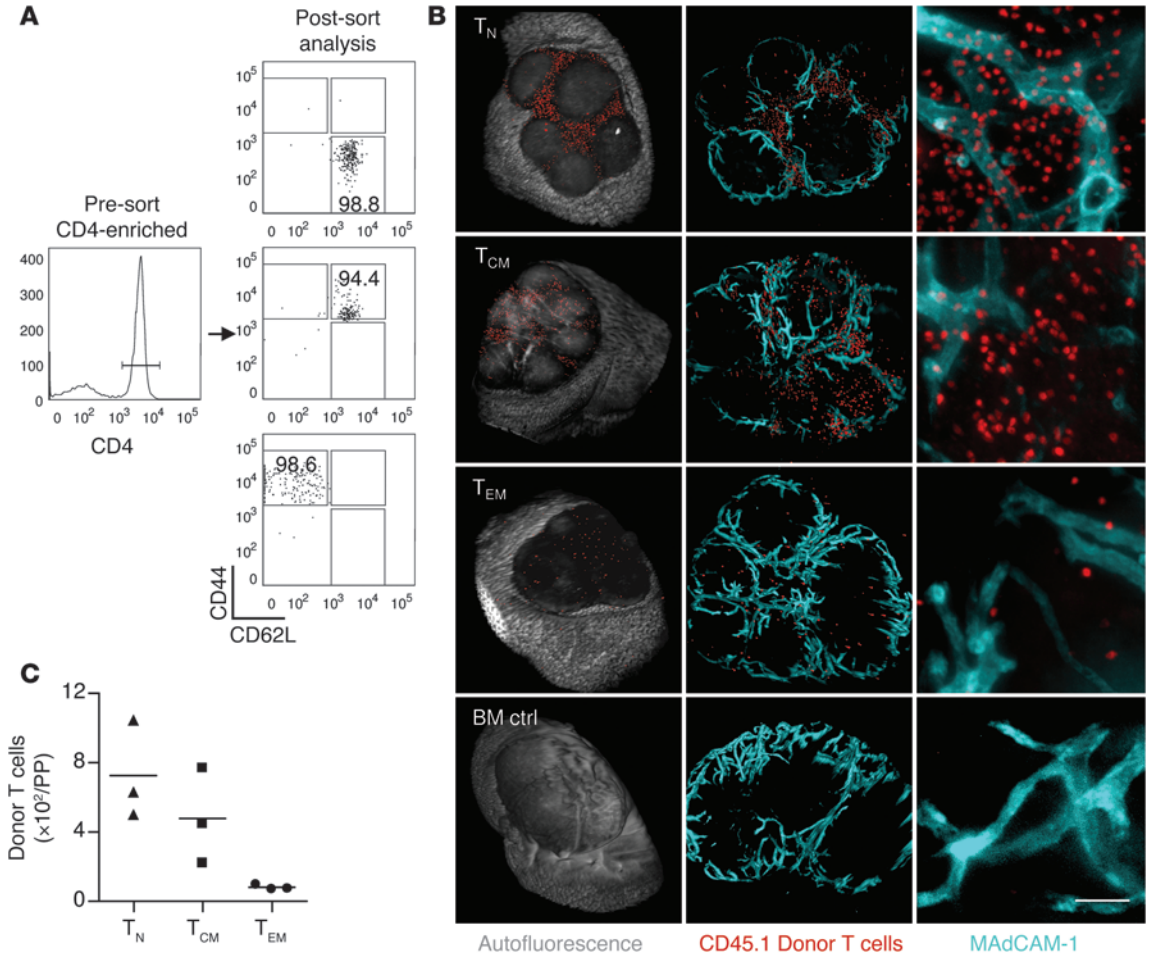

Figure 5

Detection of T cell homing by multicolor LSFM. (**A**) MACS-enriched CD4$^+$ T cells (C57BL/6-L2G85 CD45.1$^+$) were sorted into T_N (CD44^{hi}CD62L^{lo}), T_{CM} (CD44^{hi}CD62L^{hi}), and T_{EM} (CD44^{lo}CD62L^{hi}) and adoptively transferred into C57BL/6 CD45.2$^+$ recipients. (**B**) LSFM imaging of whole PPs allowed the detection of donor T cells 20 hours after transfer. Left column: 3D reconstruction of PP autofluorescence (gray) and isosurface of T cells included in the automated quantification. Center column: 3D reconstruction of MAdCAM-1$^+$ HEV (cyan) and isosurface of counted T cells (red). Right column: Representative section of the T cell area (×20, *z*-projection, scale bar: 50 μm). ctrl, control. (**C**) Quantification of transferred T cell numbers in the PPs (n = 3/group) revealed a better homing capacity of T_N and T_{CM} relative to T_{EM} cells. In contrast, T_{EM} homed more efficiently to the liver (not shown). Antibody staining was performed ex situ.

Methods

Animals and hematopoietic cell transplantation. BALB/c mice (H-2d, Thy1.2) and C57BL/6 mice (H-2b, Thy1.2) were purchased from Charles River at the age of 8–16 weeks. Transgenic mice C57BL/6.L2G85 CD90.1$^+$ expressing luciferase (luc$^+$) were generated by backcrossing the luc$^+$ FVB/N-L2G85 founder line (14) with the C57BL/6 mice for more than 12 generations. Additional transgenic luc$^+$ mice C57BL/6.L2G85 CD45.1$^+$ mice were bred in our colony. BALB/c mice were conditioned with a total body irradiation dose of 8 Gy and i.v. injected with 5 × 10^6 C57BL/6 WT sex- and age-matched bone marrow cells within 2 hours after irradiation. C57BL/6.L2G85 CD90.1$^+$ or CD45.1$^+$ magnetic bead– separated (Invitrogen) T cells (CD4/CD8 enrichment, approximately 80% purity) were coinjected to induce GVHD.

BLI. BLI was performed as previously described (13) using an IVIS Spectrum CCD imaging system (Caliper Xenogen). Mice were anesthetized with an intraperitoneally injected mixture of ketamine (50 μg/g body weight, BW) and xylazine (5 μg/g BW) in 0.1 M PBS in a total volume of 10 μl/g BW. D-Luciferin was injected at a concentration of 150 μg/g BW. Imaging data were analyzed with Living Image 4.0 (Caliper Xenogen).

Antibodies. The following murine antibodies were purchased from BioLegend and Invitrogen: CD4 (GK1.5), CD4 (RM4-5), CD8α (clone 53-6.7), CD11c (N418), CD31 (WM59), CD35 (7E9), CD44 (IM7), CD62L (MEL-14) CD90.1 (OX-7), CD45.1 (A20), CD105 (MJ7/18), CD106 (429/MVCAM.A), MAdCAM-1 (MECA-367), and podoplanin (clone 8.1.1). Human antibodies were purchased from BioLegend: CD4 (OKT4), CD8α (HIT8a), and CD31 (WM59). FACS and standard immunofluorescence microscopy were performed using an Imager Z1M (Zeiss) and a BD FACSCanto II flow cytometer (BD Biosciences).

FACS. Magnetic bead–enriched T cells were further sorted into CD4$^+$CD44^{hi}CD62L^{lo} T_{EM}, CD4$^+$CD44^{hi}CD62L^{hi} T_{CM}, and CD4$^+$CD44^{lo} CD62L^{hi} T_N using a FACSAria II cell sorter (BD Biosciences).

Preparation of mouse specimens. Organs were prepared for LSFM by modified protocols of previously described procedures (7, 31). Briefly, mice were anesthetized by intraperitoneal injection of ketamine-xylazine and transcardially perfused with 20 ml ice-cold PBS, followed by 40 ml of 4% paraformaldehyde (pH 7.4). Following the perfusion, organs were removed. The samples were placed and stored in paraformaldehyde for at least 2 hours

at 4°C until use in further procedures. Hemoglobin-rich organs were bleached for 30 minutes in 15% hydrogen peroxide/methanol. For homogenous ex situ immunofluorescence staining of large specimens, the tissue samples were blocked for 18–24 hours with 2% FCS/PBS in 0.1% Triton-X and afterward incubated with the respective antibodies for 24 hours at 4°C on a shaker, washed in PBS, incubated with streptavidin for 24 hours, and washed again in PBS, followed by dehydration in a graded ethanol series (30%, 50%, 70%, 80%, 90%, 96%, and in 100% for 2 hours each) at room temperature. After the samples were rinsed for 2 hours in 100% *n*-hexane, the *n*-hexane was replaced stepwise by a clearing solution consisting of 1 part benzyl alcohol in 2 parts benzyl benzoate (Sigma-Aldrich). Air exposure was strictly avoided at this step. Tissue specimens became optically transparent and suitable for the LSFM imaging after incubation in the clearing solution for at least 2 hours at room temperature.

In vivo antibody staining. Fluorochrome-labeled antibodies were injected i.v. 2.5 hours (300 μg CD4, CD45.1, CD90.1, or CD11c) or 0.5 hours (50 μg MAdCAM-1) before mice were euthanized. To confirm distribution and specificity of i.v. antibody staining, additional post-section staining was performed with the same antibody. To demonstrate antibody distribution and specificity of inflamed and non-inflamed tissues, CD4–Alexa Fluor 647 antibody was injected into untreated mice or into mice on day +6 after allo-HCT. Two and a half hours later, mice were euthanized, and spleens and PPs were harvested and digested according to a previously described protocol (32) with slight modifications. Briefly, organs were digested (2 mg/ml collagenase D and 0.1 mg/ml DNase I) at 37°C for 30 minutes in the presence of saturating amounts of CD4-FITC antibody (30 μg/ml) to prevent ex situ staining of remaining unbound CD4–Alexa Fluor 647. Thus, CD4-FITC single-positive cells indicate ex situ stained cells. If not specifically indicated as antibody i.v. staining, fluorescence staining was performed according to the ex situ staining protocol.

Preparation of human tissue. The preparation of human tissue required important modifications. Fresh biopsy tissue was fixed for 2–4 hours in PFA, washed in PBS, bleached in 15% hydrogen peroxide/methanol, and again washed in PBS. Subsequently, the sample was pretreated with 0.1% Triton-X/PBS for 24 hours before addition of 2% FCS for another 8 hours. To allow for homogenous staining of deeper tissue layers, antibody incubation was performed for 4–6 days in 0.1% Triton-X/PBS. After washing again in PBS, the sample was dehydrated in a graded ethanol series for 4 hours each. The clearing procedure was performed exactly as for the preparation of mouse tissue.

Multicolor LSFM. We used an LSFM setup similar to a previously described setup (8); however, the sample was illuminated from one side by various laser sources: 405-nm diode laser (56ICS025, CVI Melles Griot), 473-nm DPSS laser (MBL-473 100 mW, CNI), 532-nm DPSS laser (MGL-W532 500 mW, CNI), and 639-nm diode laser (Cube 640-40, Coherent). An objective inverter (LSM Tech) on a commercial inverted microscope (Axiovert 200, Zeiss) allowed a flexible horizontal positioning of the objective at a greater distance and range than typically possible with an inverted microscope. The laser excitation beams (3–4 mm diameter) were expanded 3-fold with a telescope (Thorlabs). With focus beam waist of 4–9 μm, an approximately 1-cm-tall light sheet was created by focusing the beam in a cylindrical lens (f = 5 cm and f = 3.6 cm, Newport) depending on the detecting objective lens (Apochromat 5× with 0.16 numerical aperture [NA] and LD Achroplan 20× with 0.4 NA objectives [Zeiss]). The beam light sheet was adjusted exactly along the focus plane of a microscope. Fine focusing of the light sheet on the specimen was performed by moving the cylindrical lens mounted on a translation stage (Standa).

After sample fixation and clearing, the specimen was affixed with Pattex acrylamide glue (Henkel) to a home-built glass rod and placed in a home-built coverglass chamber filled with clearing solution. The sample was positioned with a stepper motor–controlled stage (Standa). The stage with a feedback memory system enabled translational and rotational step motion with accuracy of 0.1 μm and 0.1 degrees, respectively.

The fluorescence emission light was filtered using a motorized filter wheel (Standa) according to the excitation wavelength: DAPI 405 nm HQ440/40, Alexa Fluor 488 (Invitrogen) 488 nm HQ525/50, Alexa Fluor 532 (Invitrogen) HQ605/75, Alexa Fluor 647 (Invitrogen) 640 nm HQ695/55 (all Chroma). Fluorescence was detected by a back-illuminated electron multiplying charge-coupled device (EMCCD) camera (512 × 512 pixels, 16 μm/pixel Cascade II, Photometrics). Exposure times for image acquisition were 200–500 ms per frame. To acquire the complete image stack, each excitation wavelength and emission filter combination was used sequentially plane by plane. We used the software package LabView (National Instruments) to control all hardware, including the synchronization with data acquisition software MetaMorph 7.1 (Molecular Devices). Finally, the individual color stacks were overlaid via image processing using the Volocity software package (PerkinElmer).

Image acquisition and processing. We acquired multicolor stacks, imaging each plane sequentially by each wavelength and emission filter combination. Stacks were taken in increments of either 1, 2, or 5 μm. Exposure times for image acquisition were 200 or 500 ms per frame. The excitation wavelengths, emission filter colors, data acquisition, and storage were synchronized by LabView software (National Instruments) and administered using the software package MetaMorph 7.1 (Molecular Devices). Resulting multicolor stacks were processed, if necessary (e.g., cropped or reduced), with ImageJ (NIH). Subsequently, we used the 3D image processing software Volocity (PerkinElmer) to prepare the individual images and videos.

MPM. Samples were embedded into a self-constructed chamber for MPM. The MPM was equipped with an optical parametric oscillator (OPO, APE) for two-photon irradiation at 1,100 nm. The excitation beam was focused with a ×20 NA 0.95 water objective (Olympus). Emission was detected with HQ535/50-nm, HQ605/70-nm, and HQ710/75-nm filters. Sequential 3D stacks were obtained for up to 1-mm penetration depth at a step size of 5 μm. Single-color image stacks (overlap, 16%) were stitched together, image size was reduced from 5,566 × 3768 pixels to 756 × 512 pixels, and photomultiplier tube–induced (PMT-induced) noise outliers were removed with ImageJ (processing package Fiji, NIH) before 3D image processing with Volocity.

Volume calculations and automated cell counting. Multicolor stacks were processed on Volocity software (Improvision) for 3D rendering and subsequently volume quantification and cell counting. We calculated volumes of autofluorescence, MAdCAM-1, and clustered donor T cells (Volocity measurements: find objects using intensity > clip objects to ROI) within a 3D ROI fitted to border the whole PP. The lower limit of specific threshold intensity was calculated with ImageJ by the mean of 10 individual threshold measurements for each individual sample. For automated cell counting, we used the following algorithm: Volocity measurements: find objects using intensity > exclude objects touching edge of image > exclude objects by size > filter measurements: standard deviation. The lower limit of the object size was set to 400 μm^2 as calculated before. We used a lower limit of the standard deviation ranging from 250 to 500 to ensure automated event identification. Mathematical analysis was performed with Excel (Microsoft) and statistical analysis with Prism 5 and InStat3 (GraphPad).

Study approval. All animal studies were performed according to specific animal use protocols approved by Regierung von Unterfranken, State of Bavaria, Germany. All biopsy samples were obtained for diagnostic purposes and after written informed consent was obtained from donors. The study was approved by the Ethics Committee of the Medical Faculty, University of Würzburg, Würzburg, Germany.

Acknowledgments

We thank F. Schwab for technical help with irradiation experiments and M. Grether for technical assistance. For critical review

of the manuscript, we thank J. Baker, G.F. Beilhack, and A.J. Wagers. This work was supported by grants to A. Beilhack from the Deutsche José Carreras Leukämie-Stiftung e.V. (DJCLS R 08/07), by the DFG (SFB TR52, Z2 and CRU216, TP4), and the Interdisziplinäres Zentrum für Klinische Forschung (IZKF) Würzburg. Additional support was provided by grants to S. Schulz from the DFG (SCHU 1518/2-1, TR36 Z2) and the Anton und Petra Ehrmann Stiftung (APES).

Received for publication May 31, 2012, and accepted in revised form September 13, 2012.

Address correspondence to: Andreas Beilhack, IZKF Research Group, Department of Medicine II, Center for Experimental Molecular Medicine, ZEMM — Zinklesweg 10, D-97078 Würzburg, Germany. Phone: 49.931.201.44040; Fax: 49.931.201.27639; E-mail: beilhack_a@klinik.uni-wuerzburg.de.

1. Gross S, Moss BL, Piwnica-Worms D. Veni, vidi, vici: in vivo molecular imaging of immune response. *Immunity*. 2007;27(4):533–538.
2. Reinhardt RL, Khoruts A, Merica R, Zell T, Jenkins MK. Visualizing the generation of memory CD4 T cells in the whole body. *Nature*. 2001; 410(6824):101–105.
3. Machnik A, et al. Macrophages regulate salt-dependent volume and blood pressure by a vascular endothelial growth factor-C-dependent buffering mechanism. *Nat Med*. 2009;15(5):545–552.
4. Sharpe J, et al. Optical projection tomography as a tool for 3D microscopy and gene expression studies. *Science*. 2002;296(5567):541–545.
5. Boppart SA, Brezinski ME, Bouma BE, Tearney GJ, Fujimoto JG. Investigation of developing embryonic morphology using optical coherence tomography. *Dev Biol*. 1996;63(0144):54–63.
6. Huisken J, Swoger J, Del Bene F, Wittbrodt J, Stelzer EHK. Optical sectioning deep inside live embryos by selective plane illumination microscopy. *Science*. 2004;305(5686):1007–1009.
7. Dodt HU, et al. Ultramicroscopy: three-dimensional visualization of neuronal networks in the whole mouse brain. *Nat Methods*. 2007;4(4):331–336.
8. Ermolayev V, et al. Ultramicroscopy reveals axonal transport impairments in cortical motor neurons at prion disease. *Biophys J*. 2009;96(8):3390–3398.
9. Ertürk A, et al. Three-dimensional imaging of the unsectioned adult spinal cord to assess axon regeneration and glial responses after injury. *Nat Med*. 2011;18(1):166–172.
10. Santi P, Johnson SB, Hillenbrand M, GrandPre PZ, Glass TJ, Leger JR. Thin-sheet laser imaging microscopy for optical sectioning of thick tissues. *Biotechniques*. 2009;46(4):287–294.
11. Kumar V, et al. Global lymphoid tissue remodeling during a viral infection is orchestrated by a B cell-lymphotoxin-dependent pathway. *Blood*. 2010;115(23):4725–4733.
12. Drexler W, Fujimoto JG. State-of-the-art retinal optical coherence tomography. *Prog Retin Eye Res*. 2008;27(1):45–88.
13. Beilhack A, et al. Prevention of acute graft-versus-host disease by blocking T-cell entry to secondary lymphoid organs. *Blood*. 2008; 111(5):2919–2928.
14. Beilhack A, et al. In vivo analyses of early events in acute graft-versus-host disease reveal sequential infiltration of T-cell subsets. *Blood*. 2005; 106(3):1113–1122.
15. Sallusto F, Lenig D, Förster R, Lipp M, Lanzavecchia A. Two subsets of memory T lymphocytes with distinct homing potentials and effector functions. *Nature*. 1999;401(6754):708–712.
16. Wagers AJ, Sherwood RI, Christensen JL, Weissman IL. Little evidence for developmental plasticity of adult hematopoietic stem cells. *Science*. 2002; 297(5590):2256–2259.
17. Al-Hajj M, Wicha MS, Benito-Hernandez A, Morrison SJ, Clarke MF. Prospective identification of tumorigenic breast cancer cells. *Proc Natl Acad Sci U S A*. 2003;100(7):3983–3988.
18. Hamann A, Jablonski-Westrich D, Jonas P, Thiele HG. Homing receptors reexamined: mouse LECAM-1 (MEL-14 antigen) is involved in lymphocyte migration into gut-associated lymphoid tissue. *Eur J Immunol*. 1991;21(12):2925–2929.
19. Szabo MC, Butcher EC, McEvoy LM. Specialization of mucosal follicular dendritic cells revealed by mucosal addressin-cell adhesion molecule-1 display. *J Immunol*. 1997;158(12):5584–5588.
20. Boscacci T, et al. Comprehensive analysis of lymph node stroma-expressed Ig superfamily members reveals redundant and nonredundant roles for ICAM-1, ICAM-2, and VCAM-1 in lymphocyte homing. *Blood*. 2010;116(6):915–925.
21. Anderson BE, et al. Memory CD4 + T cells do not induce graft-versus-host disease. *J Clin Invest*. 2003; 112(1):101–108.
22. Chen BJ, Cui X, Sempowski GD, Liu C, Chao NJ. Transfer of allogeneic CD62L- memory T cells without graft-versus-host disease. *Blood*. 2004; 103(4):1534–1541.
23. Dutt S, et al. Naive and memory T cells induce different types of graft-versus-host disease. *J Immunol*. 2007;179(10):6547–6554.
24. Anderson BE, et al. Effects of donor T-cell trafficking and priming site on graft-versus-host disease induction by naive and memory phenotype CD4 T cells. *Blood*. 2008;111(10):5242–5251.
25. Gunn MD, Tangemann K, Tam C, Cyster JG, Rosen SD, Williams LT. A chemokine expressed in lymphoid high endothelial venules promotes the adhesion and chemotaxis of naive T lymphocytes. *Proc Natl Acad Sci U S A*. 1998;95(1):258–263.
26. Huisken J, Stainier DYR. Even fluorescence excitation by multidirectional selective plane illumination microscopy (mSPIM). *Opt Lett*. 2007; 32(17):2608–2610.
27. Keller PJ, et al. Fast, high-contrast imaging of animal development with scanned light sheet-based structured-illumination microscopy. *Nat Methods*. 2010;7(8):637–642.
28. Friedrich M, Gan Q, Ermolayev V, Harms GS. STED-SPIM: stimulated emission depletion improves sheet illumination microscopy resolution. *Biophys J*. 2011;100(8):L43–L45.
29. Hama H, et al. Scale: a chemical approach for fluorescence imaging and reconstruction of transparent mouse brain. *Nat Neurosci*. 2011; 14(11):1481–1488.
30. Leischner U, Schierloh A, Zieglgänsberger W, Dodt H-U. Formalin-induced fluorescence reveals cell shape and morphology in biological tissue samples. *PloS One*. 2010;5(4):e10391.
31. Spalteholz W. Über das Durchsichtigmachen von menschlichen und tierischen präparaten. Leipzig, Germany: S. Hierzel; 1914.
32. Galkina E, Thatte J, Dabak V, Williams MB, Ley K, Braciale TJ. Preferential migration of effector $CD8^+$ T cells into the interstitium of the normal lung. *J Clin Invest*. 2005;115(12):3473–3483.